# Improved PV Inverter Operating Range Using a Miniboost

Emanuel Serban, *Senior Member, IEEE*, Francisco Paz, *Student Member, IEEE*, and Martin Ordonez, *Member, IEEE*

***Abstract*—In the past two decades, the operating voltage of photovoltaic (PV) installation has increased in order to reduce current ratings and system installation costs. Such a large number of PV panels in series (e.g., 1000–1500 V systems) lead to wide variations of PV voltage due undesirable effects such as shading, soiling/dust, aging, and hot surface temperature. A partial shade would normally shut down solar inverters, unless a boost stage is added to the system input to ensure a proper dc-link operating voltage for the inverter. A boost input stage can double the input voltage operating range to extract maximum power under any possible shading and temperature condition. In this paper, a new PV string boost topology arrangement is proposed in the form of a miniboost used for three-phase grid-connected converters. The string miniboost increases the dc voltage range to extend power extraction under shading and low irradiance conditions and only requires to process a fraction of the rated power. The proposed cost-effective solution is further improved by using the inverter peak power envelope at boundary operation, resulting in expanded energy extraction beyond existing techniques. A design procedure to optimally size the miniboost and the peak-power envelope is presented along with a comparative analysis, under different irradiance levels, to illustrate the advantages in energy extraction obtained with the proposed PV string miniboost solution under low voltage and boundary operation. Furthermore, improved efficiency operation schemes and issues of common-mode current are discussed, and three mitigation design techniques intended for three-phase, three-level inverter transformerless topology are presented. Simulations and experimental results using a dual miniboost dc–dc stage and three-phase three-level neutral point clamped inverter are presented to validate the proposed dc-bus extension range and system design.**

***Index Terms*—DC-bus voltage utilization, leakage currents, peak power maximum power point tracking (MPPT), photovoltaic (PV) energy production, PV string boost design optimization.**

## I. Introduction

TRANSFORMERLESS grid-connected photovoltaic (PV) inverters present the merits of high efficiency and density to perform renewable energy production and power conversion. The most common roof-top residential and commercial PV installations are designed for operation under 1000 V open-circuit voltage due to safety regulations and system component ratings [1]. The inverter may operate up to 850 $V_{\rm dc}$ ($V_{\rm dcMax}$) at full nominal power ($P_{{\rm dc}N}$) and extend the range up to 1000 $V_{\rm dc}$ ($V_{\rm ov}$) with reduced power operation due to limited voltage/power characteristics of commercially available power devices [2]–[4]. Single-stage converters operate from a minimum dc voltage ($V_{\rm dcMin}$) that is in relation to the grid voltage and below this value, the inverter does not produce power. This challenge can be mitigated by introducing a boost input stage that converts the voltage of the panel to the required rated bus voltage. This approach requires the addition of a second power stage with nominal power rating ($P_{{\rm dc}N}$) so cost considerations and efficient operation are critical. Grid-connected PV inverters require advanced power conversion control strategies to integrate and enable energy production with high efficiency, power quality, and reliability [5]–[9].

Modern PV power plants have been studied in the literature including energy production maximization, control strategies related to reduced irradiance and PV modules orientation [10]–[15]. The PV module manufacturer specification is given at standard test conditions (STC, 1 kW/m$^2$, 25 °C cell temperature, and air mass of 1.5). In real applications, these ideal conditions are almost simultaneously nonexistent. The negative factors which impact the PV power extraction are related to low irradiance conditions, nonoptimal tilt angles, PV cell soiling and dust, PV modules aging, and partial shading of the modules resulting in power production degradation.

Maximum power point tracking (MPPT) is one essential part of any PV application. These algorithms ensure the PV array operates at the most efficient condition, producing as much energy as possible, even under changing environmental conditions [16]–[18]. One of the main problems with MPPT algorithms is related to local maxima created by partial shading conditions [19]–[21]. Although many solutions have been proposed that tackle the issue of local maxima [22]–[26], a key problem still remains: the global maximum can be located at a voltage that is much lower than the overall voltage of the array. PV inverters with a single stage [see Fig. 1(a)] will not be able to operate at such low voltages, making the inverter useless or significantly reducing the production energy below what is available. This problem is especially important when the PV string becomes larger, leading to the presence of more operation points at local maxima.

The operating region of the typical single-stage PV grid-connected inverter is illustrated in Fig. 1(a). It is delimited by $V_{\rm dcMin}$, below which the inverter enters in nonoperational mode; above $V_{\rm dcMin}$, the inverter can operate at full $P_{{\rm dc}N}$ until $V_{\rm dcMax}$, and after that power is curtailed to extend the range to $V_{\rm ov}$; above

Manuscript received August 17, 2016; revised November 8, 2016; accepted December 13, 2016. Date of publication December 19, 2016; date of current version June 23, 2017. Recommended for publication by Associate Editor B. Singh.

The authors are with the University of British Columbia, Vancouver, BC V6T 1Z4, Canada (e-mail: emaserban@ieee.org; franciscopaz@ieee.org; mordonez@ieee.org).

Color versions of one or more of the figures in this paper are available online at http://ieeexplore.ieee.org.

Digital Object Identifier 10.1109/TPEL.2016.2641478

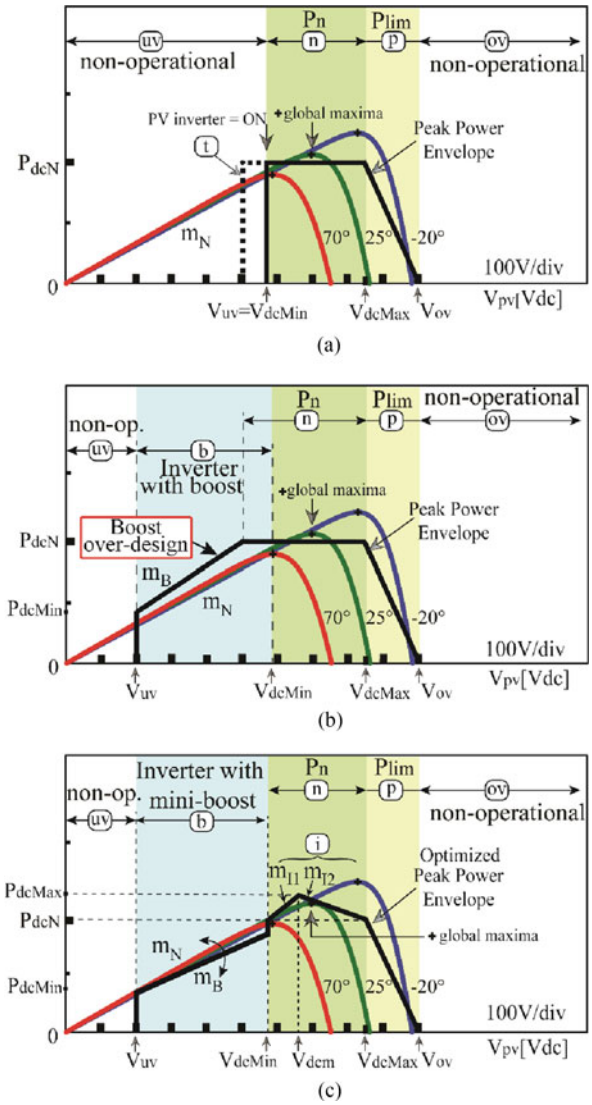


Fig. 1. PV power versus dc-bus voltage utilization characteristics for: (a) inverter without boost stage, (b) inverter with standard boost stage, and (c) proposed optimized inverter with miniboost and peak-power envelope at boundary conversion operation solution. *uv*: nonoperational under dc voltage shutdown range. *b* Operation with boost converter. *n*: nominal power operation (MPPT). *p*: power limit/curtailing mode. *ov*: overvoltage dc nonoperational (components failure). *t*: grid interfaced with line transformer for increased operational voltage (optional). *i* increased converter power, optimization for constant input PV current and constant power losses operation.

$V_{\rm ov}$, the inverter is nonoperational. This range can be extended (indicated by $(t)$) by using a transformer to interface the grid, but the weight, volume, and the efficiency are penalized. In Fig. 1(b), the two-stage power conversion PV operating region is presented. The boost power converter follows the slope $(m_b)$ that is reduced until new minimum voltage $(V_{uv})$ is achieved. Unfortunately, since the PV array will not produce the nominal power when the shades and problems cause it to operate at the lower voltage, the boost converter is overdesigned causing the cost to be unnecessary high.

The PV module's energy production reduction is attributed to several factors, including irradiance variability, partial shading, soiling, cells delamination and discoloration, and

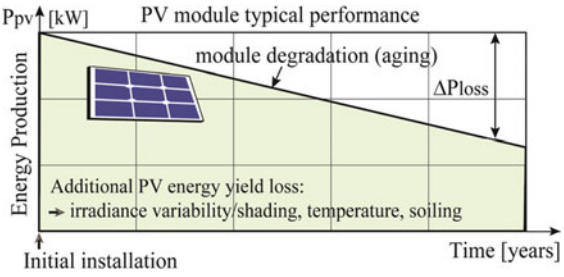


Fig. 2. Typical representation of PV energy production over time.

increased operation temperature. The use of the standard boost design would lead excess of materials (e.g., magnetics, electronic components) while not being able to benefit of its full rated power capability.

In Fig. 2, a typical representation of PV module energy production over time used by manufacturers to provide required warranty or to differentiate their performance is shown. The power loss ($\Delta P_{\rm loss}$) over time is inherent and the standard boost becomes evidently an overdesign. In contrast, the proposed PV string miniboost design leads to an improvement in energy production over time in terms of both initial cost and return of investment.

In this work, a new topology and design methodology based on a string miniboost converter at the input of the PV inverter is presented. In Fig. 1(c), an improved PV inverter operational range for power extraction and design optimization is presented using a miniboost. The boost stage converter is designed to operate only when the voltage is lower than $V_{\rm dcMin}$ and becomes disengaged when PV voltage exceeds $V_{\rm dcMin}$, for an increase in system conversion efficiency and the operation at rated power.

The proposed PV string miniboost is designed to process only a fraction of the PV inverter nominal power $P_{{\rm dc}N}$, leading to the use of smaller, and therefore lower cost components. The inverter sizing is further optimized based on a proposed peak power envelope at the boundary of the operating area. This technique allows for extra room in the operating region, to generate more power into the grid than previously possible.

Transformerless grid-connected PV systems are susceptible to leakage current generation above the required safety limits. The stray capacitance between the PV array positive and negative terminals and grounded frame provides a current circulation path among the PV source, converter, and ac grid port. In three-phase neutral point clamped (NPC) topology, the neutral point can be bonded to grid neutral in order to suppress the leakage current [27]. Modulation techniques have been proposed in three-phase systems for leakage current reduction [28]–[30]. However, with these methods, the modulation index is limited and maximum dc bus utilization cannot be achieved. In this work, three methods are discussed that minimize current leakage while maintaining the maximum dc-bus utilization.

The work is organized as follows. The characteristics of the typical grid-connected inverter (single-stage and two-stage) are presented in Section II. The advantages of the proposed topology compared with the existing ones are presented in Section III.

The design considerations for the string miniboost with peak power envelope optimization are presented in Section IV. Section V presents a case study of a PV plant designed using the proposed guidelines, and discusses issues and solutions to minimize common-mode (CM) current circulation in three-phase three-level inverter transformerless topologies. The simulation and experimental validation of the extended range, improved efficiency, and reduced leakage current of the grid-connected PV conversion system is presented in Section VI. Finally, the conclusions and observations are presented in Section VII.

## II. PV Inverter With Single- and Two-Stage Power Conversion

Fig. 1(a) and (b) shows the operating region of the two traditional PV grid-connected inverter topologies. In the following paragraphs, the details of the design and operating boundaries will be presented along with the resulting advantages and disadvantages comparison. The proposed PV string miniboost topology is presented in Section III.

### A. PV Inverter With Single-Stage Power Conversion (No Boost Converter)

The single-stage PV inverter operating area is presented in Fig. 1(a). The single-stage inverter is simple and efficient, since it does not include a second stage, but the operation is limited at the minimum operating voltage ($V_{\mathrm{dcMin}}$) that is required to synchronized to the grid voltage. The region below $V_{uv}$ represents the under voltage (*uv*) region, where the inverter is nonoperational.

A single-stage inverter may operate from $V_{\mathrm{dcMin}} = 575\,\mathrm{V}$ (lower dc-bus limit) to $V_{\mathrm{dcMax}} = 850\,\mathrm{V}$ (upper dc-bus limit) at $P_{\mathrm{dc}N}$, and extend the range up to $1000\,V_{\mathrm{dc}}$ with reduced power operation due to limited voltage blocking of commercially available power devices. The $V_{\mathrm{dcMin}}$ is dependent of the modulation strategy used as per

$$\begin{cases} V_{\mathrm{dcMin}} = 2 \cdot \hat{V}_{LN} + V_{\mathrm{dcComp}}(\mathrm{SPWM}) \\ V_{\mathrm{dcMin}} = \sqrt{3} \cdot \hat{V}_{LN} + V_{\mathrm{dcComp}}(\mathrm{ZS-PWM}). \end{cases} \tag{1}$$

The minimum dc voltage is selected considering the compensation voltage $V_{\mathrm{dcComp}}$, in addition to grid phase voltage magnitude $\hat{V}_{LN}$, ensuring the inverter operation in linear modulation. The zero-sequence (ZS) pulse-width modulation is used in this work, and provides an advantage over sinusoidal pulse-width modulation (SPWM) with an extension of $2/\sqrt{3}$ for the dc input voltage utilization. If a line transformer is interfaced between the output of converter and grid for lower ac grid voltage inverter operation (e.g., 15% lower), then, the minimum voltage can be extended to lower PV input voltage. However, adding a line transformer to the system does not provide a cost-effective solution since it increases weight, volume, and reduces efficiency [1].

### B. PV Inverter With Two-Stage Power Conversion (With the Boost Converter)

The operating region for the PV inverter with boost stage is presented in Fig. 1(b). In this case, the operating region is extended (although not at full nominal power). This topology design allows more energy to be extracted; however, its components are oversized and the efficiency is reduced. For uniform irradiance, the voltage will rarely drop below ($V_{\mathrm{dcMin}}$) and for partial shading, the available power is less than the rated power. At lower voltage levels, the inverter is able to extract the available power from the PV modules. The rated boost power at lower PV voltage is limited by the current ratings of power devices, current sensors, and magnetics. As shown in Fig. 1(b), the boost power stage is not optimized since the boundary of the operating region boot power ($P_B = V_{\mathrm{dc}} I_{\mathrm{dc}}$) is greater than the available power from PV-string modules ($P_{\mathrm{pv}}$). It can be noted that the boundary power gradient of the boost stage ($m_B$)

$$m_B = \frac{dP_B}{dV_{\mathrm{pv}}} \tag{2}$$

is greater than the gradient determined by the series/parallel combination of PV modules ($m_N$)

$$m_N = \frac{dP_{\mathrm{pv}}}{dV_{\mathrm{pv}}}. \tag{3}$$

Furthermore, considering the shading effect, the available PV power decreases further; therefore, the boost power stage is not optimized which leads to an overcost design.

The maximum recommendable design sizing criteria for PV voltage and current ($I_{\mathrm{pvMax}}$, $V_{\mathrm{pvMax}}$) are given by

$$\begin{cases} I_{\mathrm{pvMax}} = N_p I_{\mathrm{scTmax}} \le I_{\mathrm{maxAdm}} \\ V_{\mathrm{pvMax}} = N_s V_{\mathrm{ocTmin}} \le V_{\mathrm{maxAdm}} \end{cases} \tag{4}$$

where $N_p$ and $N_s$ are the number of parallel strings in the array and the number of series cells in each string, respectively, $I_{\mathrm{sc}T\mathrm{max}}$ and $V_{\mathrm{oc}T\mathrm{min}}$ are the short-circuit current at the maximum temperature $T_{\mathrm{Max}}$ and open-circuit voltage, respectively, at the minimum temperature $T_{\mathrm{Min}}$, $I_{\mathrm{maxAdm}}$ is the maximum admissible current given by the ratings of the power devices, inductors, switch-gear, and cables, and $V_{\mathrm{maxAdm}}$ is the maximum admissible voltage given by the components ratings.

It can be argued that connecting more PV stings in parallel would increase the power gradient, beyond $m_N$ .

However, an important cost-effective design criterion is the maximum short-circuit current that the switch gear and the cables can handle, which leads to selection of maximum number of PV strings parallel ($N_p$) and series ($N_s$) connected is given by

$$\begin{cases} N_p \le \dfrac{I_{\mathrm{maxAdm}}}{I_{\mathrm{scTmax}}} \\ N_s \le \dfrac{V_{\mathrm{maxAdm}}}{V_{\mathrm{ocTmin}}}. \end{cases} \tag{5}$$

In this context, it is clear that the boost stage has been dimensioned for the full rated power $P_{\mathrm{dc}N}$, although it will only ever

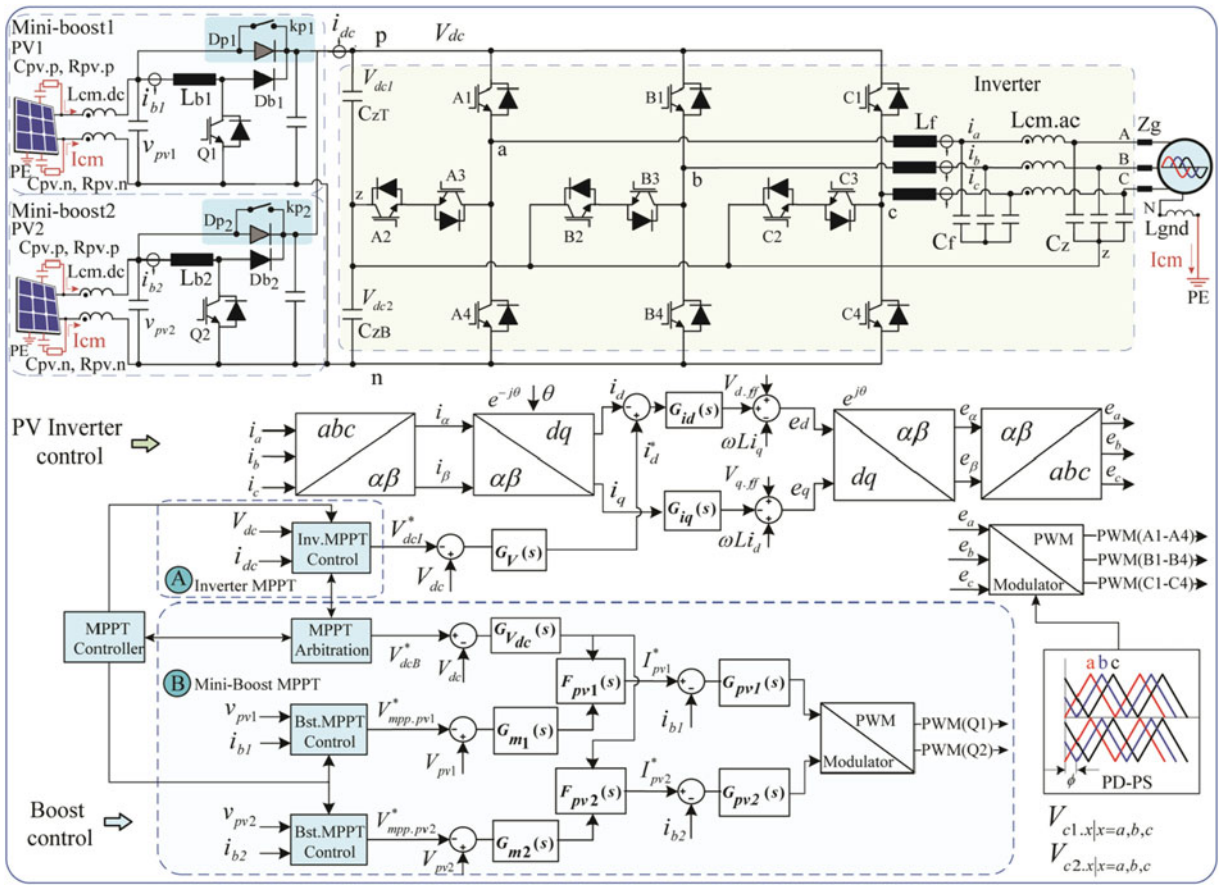


Fig. 3. Power conversion stage and control block diagram with miniboost engagement at low PV voltage operation. The maximum power point is determined by the MPPT block algorithm, that shifts control from the PV inverter to the miniboost stages under different operating conditions.

process a fraction in it. Therefore, the implementation through the traditional approach results in an overdesigned solution.

## III. PV Inverter With the Proposed PV String Miniboost

A novel approach solution is presented in Fig. 1(c): the miniboost stage with peak power envelope boundary operation. In this case, a boost stage is included that is designed for a fraction of the rated power of the PV inverter and that can be bypassed if the PV array can provide the voltage by itself.

This solution offers a tradeoff between the single-stage converter and the two-stage converter, offering the benefits of both parts without the additional losses and cost of a full size boost. When large PV plants are considered, the miniboost stages can be distributed to each string and rated for a fraction of each strings power.

A schematic of the proposed topology is included in Fig. 3. In this schematic, two strings are included in the PV array, and each string is assigned to a miniboost, dc–dc conversion. The dc–ac power stage conversion is implemented using a three-level NPC PV inverter. Each dc–dc miniboost stage is built using an inductor, a capacitor, a switch ($Q_1, Q_2$), and a diode ($D_{b1}, D_{b2}$) while the stage can be bypassed using diode $D_{p1}, D_{p2}$ when the boosting is not needed. Conversely, if $D_{p1}, D_{p2}$ are not implemented, the current flows through two series elements: a boost inductor ($L_{b1}/L_{b2}$) and a boost diode ($D_{b1}/D_{b2}$—silicon carbide) which leads to additional losses. Instead, the bypass diodes $D_{p1}, D_{p2}$ are selected with a low voltage-drop and low-cost standard recovery silicon-type rectifiers. Furthermore, the replacement of the bypass diode with an even lower on-resistance switch ($k_{p1}, k_{p2}$, e.g., low-cost relay) will result in lower losses and heat dissipation. A simple control signal between $k_{p1}, k_{p2}$, and $Q_1, Q_2$ is implemented with a mutually exclusive logic. Therefore, the proposed redesign of the bypass boost switch provides an opportunity for higher efficiency operation, as will be demonstrated in Section VI.

The combined output of the miniboost stages is connected to dc link, $V_{\rm dc}$, which represents the input voltage for the dc–ac inverter power stage. The three-phase inverter topology selection is a three-level T-type NPC as shown in Fig. 3. The inverter three-phase currents from natural *abc* coordinates $i_a$, $i_b$, $i_c$ are transformed to stationary $\alpha\beta$-frame, $i_\alpha$, $i_\beta$, which are then converted to synchronously rotating reference *dq*-frame $i_d$, $i_q$, as shown in Fig. 3. The grid-connected converter (miniboosts and inverter) MPPT active power is achieved by the active current controller $G_{id}$ with feedforward grid voltage *d*-axis component $\hat{V}_{LN} = V_d$ and decoupling from *d*-axis with the cross-coupling term $\omega L i_q$. The peak power envelope inverter operation is determined by the active current component ($i_d$) generated to the grid network. The active current reference $i_d^*$ is obtained from

TABLE I
GRID-CONNECTED INVERTER WITH- AND WITHOUT BOOST PV SYSTEM COMPARISON SUMMARY

| Criterion | Inverter without boost | Inverter with standard boost | Inverter with PV string miniboost |
|---|---|---|---|
| MPPT range (dc-ratio) | Reduced | Improved | Optimized |
| System cost/W | Reduced | High | Medium/Optimized |
| System weight/power density | Reduced | Standard | Medium/Optimized |
| PV system power production at low irradiance levels | Restricted (e.g.$< V_{\mathrm{MPP}}, P_{\mathrm{lim}}$) | Improved (e.g. $V_{\mathrm{MPP}}, P_{\mathrm{MPP}}$) | Optimized (e.g. $V_{\mathrm{MPP}}, P_{\mathrm{MPP}}$) |
| Operation voltage at high PV cell temperature (MPP locus) | Restricted (e.g.$< V_{\mathrm{MPP}}, P_{\mathrm{lim}}$) | Improved (e.g. $V_{\mathrm{MPP}}, P_{\mathrm{MPP}}$) | Optimized (e.g. $V_{\mathrm{MPP}}, P_{\mathrm{MPP}}$) |
| PV string design flexibility due to extreme temperature conditions | Restricted | Improved | Optimized |
| PV power system application: ground mounted, residential/commercial roof-top, car-ports | Restricted | Optimized | Optimized |
| PV inverter design | Reduced | Complex | Complex |

the dc-link voltage regulator $G_V$ :

$$i_d^* = (V_{\mathrm{dc}} - V_{\mathrm{dc}I}^*)G_V. \tag{6}$$

The inverter dc-link voltage reference $V_{\mathrm{dc}I}^*$ is a programmed value determined by the MPPT controller. The inverter MPPT active power is controlled by the equivalent inverter output average voltage $e_d$ given by

$$\begin{cases} e_d = V_d - \omega L i_q + (i_d^* - i_d)G_{id} \\ e_q = V_q + \omega L i_d - i_q G_{iq}. \end{cases} \tag{7}$$

Fig. 3 also shows the proposed control and MPPT implementation of the system. As it can be observed, the MPPT algorithm block is not only in charge of determining the MPP but also of moving back and forth between the single-stage and two-stage topologies. Eq. (8) shown at the bottom of this page.

The arbitration of MPPT algorithm-control between the string miniboosts and inverter power stages is performed as per relation (8).

The MPPT controller (see Fig. 3) selects the execution of maximum power tracking according to (8). In addition, the selection functions $F_{\mathrm{pv}1},\ F_{\mathrm{pv}2}$ determine the boost current references $I_{\mathrm{pv}1}^*,\ I_{\mathrm{pv}2}^*$, where in normal operation, these functions use the output of $G_{m1},\ G_{m2}$ control blocks. However, in a grid fault case scenario, the selection functions use the output of the $G_{V\,\mathrm{dc}}$ controller which must regulate the dc-link voltage at the reference voltage established by $V_{\mathrm{dc}B}^*$.

A comparison summary for a grid-tie inverter with standard boost, without and with miniboost power stage, is presented in Table I. It can be seen that the proposed PV string miniboost topology introduces improvements in almost all the aspects compared in the table, which represent the main concerns when designing a power inverter for PV applications.

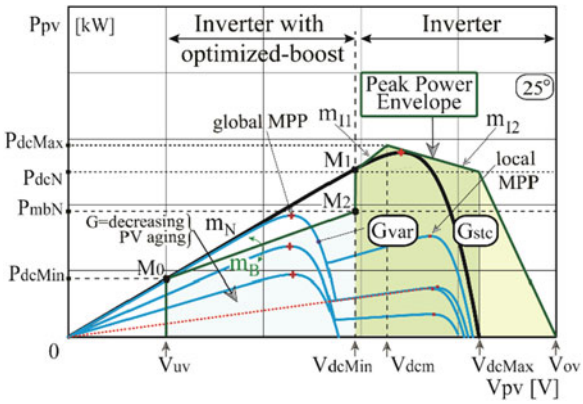


Fig. 4. *P–V* characteristics under STC uniform insolation ($G_{\mathrm{stc}}$) and two-step partially shaded ($G_{\mathrm{var}}$) operating conditions for boost design optimization. This shading profile is used to obtain the miniboost characteristics.

## IV. DESIGN OF THE MINIBOOST STAGE WITH PEAK POWER ENVELOPE OPTIMIZATION

The renewable power that can be utilized and delivered to the ac grid, using an inverter with an optimized miniboost power stage, is illustrated in Fig. 4. This design adds two major new features: the PV string miniboost topology and the peak power envelope optimization. The design procedure for the proposed architecture will be outlined in the following paragraphs.

### A. PV String Miniboost Stage Design

The design of the miniboost is based on selecting a power rating and gradient ($m_b$) that will be enough to tackle the power of the inverter at when the voltage has dropped below $V_{\mathrm{dcMin}}$ and no more. The boost boundary power gradient ($m_B$) is designed to be less than or equal to the gradient of the PV-string ($m_N$), considered at STC.

$$\begin{cases} \text{a.MPPTisperformedbytheinverter} & \text{if } (V_{\mathrm{pv}1} \text{ and } V_{\mathrm{pv}2}) > V_{\mathrm{dcMin}} \\ \text{b.MPPTisperformedbyeachminiboost} & \text{if } (V_{\mathrm{pv}1} \text{ and } V_{\mathrm{pv}2}) < V_{\mathrm{dcMin}} \\ \text{c.MPPTisperformedbyoneminiboostandinverter} & \text{if } (V_{\mathrm{pv}1} \text{ or } V_{\mathrm{pv}2}) < V_{\mathrm{dcMin}}. \end{cases} \tag{8}$$

A convenient design consideration is that the $m_N$ of the PV modules is practically independent of the operating cell temperature, as can be seen from Fig. 1.

The linearity of *P–V* characteristics and the close matching curves below MPP voltage determines the sizing boost selection criteria

$$m_B \leq m_N. \tag{9}$$

The minimum dc ($P_{\mathrm{dcMin}}$) power is less than the MPP voltage ($V_{MP}$) at the same power gradient

$$P_{\mathrm{dcMin}} = m_B V_{uv} < I_{\mathrm{MPP}} V_{\mathrm{MPP}} \tag{10}$$

where in a practical design, the minimum miniboost start-up voltage ($V_{uv}$) is correlated with the internal auxiliary supply

$$V_{uv} = V_{\mathrm{auxMin}} + V_{\mathrm{offset}}. \tag{11}$$

The string boost is designed for the power size considering (4), (5), (7)–(9). At low irradiance levels, the boost extracts the available energy from the PV string modules. The string boost sizing design optimization methodology is proposed as follows.

1) $N_p, N_s$: select the number of series and parallel PV modules (e.g., using (5)).
2) $m_N$: determine power gradient of the PV modules given by the equation of the line $(M_0, M_1)$. The maximum boost size is less or equal to the nominal inverter rated power (e.g. $P_{mbN} \leq P_{\mathrm{dcN}}$).
3) $m_B$: calculate the boost boundary power gradient using (10).
4) $P_{mbN}$: the selection of miniboost boundary power is suggested within a range, with a maximum power selected at $M_1(V_{\mathrm{dcMin}}, P_{\mathrm{dcN}})$, Fig. 4. However, the miniboost maximum power can be selected at a lower value, $M_2(V_{\mathrm{dcMin}},\ P_{mbN})$, Fig. 4. This is selected based on the shading profile, components cost design optimization, and PV modules aging-degrading prediction. The boost component cost reduction aims for design optimization in cooling, magnetics, current sense transducer, and power semiconductor devices.

The PV voltage variation with the MPPT control arbitration between the boosts and inverter power stages among the inverter, miniboost, and hybrid cases is shown in Fig. 5. The proposed string miniboost provides an advantage over the standard solution, in the optimization for cost, size, and power density. During the tracking process, when the PV voltage ramps above $V_{\mathrm{dcInv}}$, the PV inverter transitions to operate without the miniboost stage (boost disengaged) and the MPPT control moves to the inverter stage (*n*-region). When the operating voltage drops below $V_{\mathrm{dcInv}}$, the boost is turned on again and the MPPT is transferred to the miniboost stage (*b*-region).The PV operating range of the string boost and inverter power ratings can be

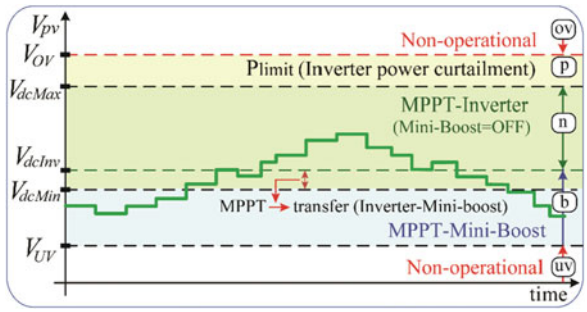


Fig. 5. Inverter input dc voltage control by the MPPT algorithm; when the PV voltage is lower than the minimum voltage of the single-stage PV inverter, the boost stage is engaged and the MPPT control shifts to the miniboost stage with peak power envelope operation. $V_{UV}$: nonoperational dc under voltage (*uv*, e.g., 200 Vdc). $V_{\mathrm{dcMin}}$: minimum dc-link voltage for inverter operation in linear modulation range (per (1)). $V^*_{\mathrm{dc}I}$: dc-link reference voltage under inverter–MPPT control mode. $V^*_{\mathrm{dc}B}$: dc-link reference voltage under boost voltage regulation mode. $V_{\mathrm{OV}}$: Nonoperational dc over voltage (*ov*, e.g., 1000 Vdc).

described through the following expression:

$$P_{\mathrm{inv}}(V_{\mathrm{pv}}) = \begin{cases} P_b(V_{\mathrm{pv}}) = \begin{cases} I_{\mathrm{MP}} V_{\mathrm{pv}} \text{ if } V_{uv} \leq V_{\mathrm{pv}} \leq V_{\mathrm{MP}} \\ P_{mbN} \text{ if } V_{\mathrm{MP}} \leq V_{\mathrm{pv}} \leq V_{\mathrm{dcMax}} \end{cases} \\ P_{mbN} \cdot \left(1 - \frac{V_{\mathrm{pv}} - V_{\mathrm{dcMax}}}{V_{\mathrm{ov}} - V_{\mathrm{dcMax}}}\right) \text{ if } V_{\mathrm{dcMax}} \leq V_{\mathrm{pv}} < V_{\mathrm{ov}} \\ 0 \text{ if } V_{\mathrm{pv}} \geq V_{\mathrm{ov}}. \end{cases} \tag{12}$$

The string boost is designed with an adaptive duty-ratio, function of the grid ac voltage and is expressed as follows:

$$D(V_{\mathrm{pv}}, V_{\mathrm{ac}}) = 1 - \frac{V_{\mathrm{pv}}}{V_{\mathrm{dc}}(V_{\mathrm{ac}})}. \tag{13}$$

In this case, the inverter control establishes the dc-bus regulation level ($V^*_{\mathrm{dc}I}$, Fig. 3), which is adaptive to the grid voltage variations (e.g., line voltage $400\tilde{}\mathrm{V}_{\mathrm{ac}} \pm 15\%$). As a result, two immediate benefits are established: 1) lower boost duty-ratio $D(V_{\mathrm{pv}}, V_{\mathrm{ac}})$ operation leads to higher efficiency; and 2) the inverter performs with higher efficiency at lower dc-bus voltage range, as will be demonstrated by the measured efficiency in the experimental section.

Fig. 6 shows the boost and inverter operating range derived from (12) and (13) and the PV current drawn from the PV array, $I(V_{\mathrm{pv}}) = P_b(V_{\mathrm{pv}})/V_{\mathrm{pv}}$.

### *B. Peak Power Envelope Optimization*

An additional proposed optimization criterion is the power conversion system design selection at peak power envelope boundary operation. The inverter power stage is designed for operation over its rated power ($P_{\mathrm{dcMax}} > P_{\mathrm{dcN}}$). The $P_{\mathrm{dcN}}$ represents the inverter nominal MPPT power and is selected at maximum dc voltage ($V_{\mathrm{dcMax}}$), where the inverter exhibits the higher conversion losses (due to increased power devices switching losses and core magnetics losses). $P_{\mathrm{dcMax}}$ represents the maximum inverter MPPT power, operation at optimum dc input voltage ($V_{\mathrm{dc}m}$) where the conversion losses are lower than at the maximum voltage $V_{\mathrm{dcMax}}$.

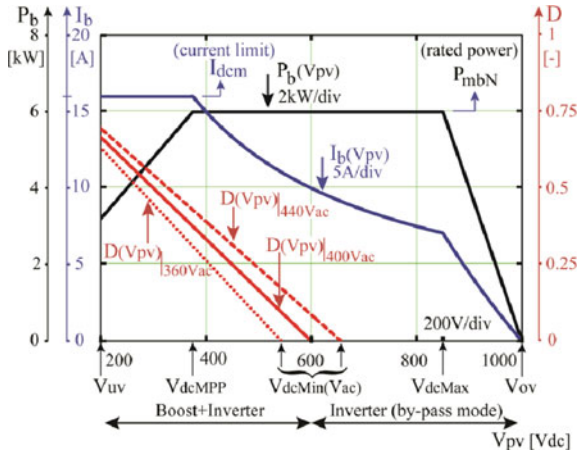


Fig. 6. Grid-connected system operating range: boost rated power ($P_b$), input current ($I_b$), and duty-ratio as a function of PV voltage.

The inverter MPPT power operation is designed for two intervals, given by

$$\begin{cases} m_{I1} = \frac{\Delta P_{I1}}{\Delta V_{\mathrm{pv1}}} > 0 \\ m_{I2} = \frac{\Delta P_{I2}}{\Delta V_{\mathrm{pv2}}} < 0. \end{cases} \tag{14}$$

During the first interval, the inverter operates with constant current

$$I_{\mathrm{dc}m} = \frac{P_{\mathrm{dcInv}}}{V_{\mathrm{dcMin}}} = \frac{P_{\mathrm{dcMax}}}{V_{\mathrm{dc}m}} \tag{15}$$

and the dc power can increase linearly to $P_{\mathrm{dcMax}}$

$$\begin{cases} \Delta P_{I1} = P_{\mathrm{dcMax}} - P_{\mathrm{dcInv}} \\ \Delta V_{\mathrm{pv1}} = V_{\mathrm{dcm}} - V_{\mathrm{dcMin}}. \end{cases} \tag{16}$$

At the beginning of second interval, the dc power decreases linearly toward $P_{\mathrm{dc}N}$ due to increase in power losses

$$\begin{cases} \Delta P_{I2} = P_{\mathrm{dcMax}} - P_{\mathrm{dcN}} \\ \Delta V_{\mathrm{pv2}} = V_{\mathrm{dcMax}} - V_{\mathrm{dcm}}. \end{cases} \tag{17}$$

The inclusion of these power gradients in the inverter operating area optimizes the utilization of the inverter power semiconductors. Instead of taking the conservative approach and defining the operating limit all through $V_{\mathrm{dcMin}}$ to $V_{\mathrm{dcMax}}$ as $P_{\mathrm{dc}N}$ (which is only true at $V_{\mathrm{dcMax}}$), a more realistic approach is presented that has the benefit of being shaped as the *P–V* curve of the panel, adding operating region where it is most needed.

## V. PV System Operation Case Study

### A. PV String Miniboost Stage Design Considerations Using P–V Characteristics

A solar array power installation is designed with PV modules connected in series–parallel configuration in order to ensure the desired working voltage and current within the power system. The PV array maximum open-circuit voltage is calculated at the lowest daily minimum temperature (with PV module voltage temperature coefficient $\beta$) and maximum-power point voltage ($V_{\mathrm{mp}}$) for the PV array string is determined at the daily PV cell temperature ($T_c$), with the consideration of STC of $1000\,\mathrm{W/m^2}$ irradiance and $T_{\mathrm{stc}} = 25\,^{\circ}\mathrm{C}$ reference temperature

$$\begin{cases} V_{\mathrm{oc}} = V_{\mathrm{oc.stc}}\left[1+\beta_{V_{\mathrm{oc}}}\left(T_c - T_{\mathrm{stc}}\right)\right] \\ V_{\mathrm{mp}} = V_{\mathrm{mp.stc}}\left[1+\beta_{V_{\mathrm{mp}}}\left(T_c - T_{\mathrm{stc}}\right)\right]. \end{cases} \tag{18}$$

As per (4), (5), and (18), the selection of number of series ($N_s$) connected PV modules is maximized up to the $V_{\mathrm{ocAdm}}$ (with the constraint of $V_{\mathrm{oc.max}} = 1000\,\mathrm{V}$) calculated at the lowest ambient temperature (e.g., $T_{\mathrm{min}} = -20\,^{\circ}\mathrm{C}$). The selection of parallel ($N_p$) connected PV modules is selected based on grid-tie converter availability, cable sizing, and maximum short-circuit switch-gear capability. Using (4) and (18), the series- and parallel-connected PV modules are $N_s = 19$, respectively, $N_p = 2$.

In this case, the proposed string miniboost design considers the use of up to two strings connected in parallel ($N_{P\mathrm{max}} = 2$) for the balance-of-systems cost reduction due to fuse elimination (cost reduction), the higher MPPT granularity, and the arc-fault detection that can use the same current sensors used in the miniboost control.

The over-sizing power ratio selection (e.g. $P_{\mathrm{pv}}/P_{\mathrm{dc}N} = 1.2$) between PV array and electronic converter (i.e. boost, inverter) is dependent on project location including tilt angle, orientation, dc switchgear, wiring losses. Safety regulations and standards imposes design margins, in addition to oversizing ratio, for cables, bus bars, switchgear which further leading to increased system cost. Therefore, the oversizing power ratio is practically limited and the proposed string miniboost stage provides an improved and optimized solution.

The PV array strings are prone to nonuniform solar irradiance, and the cases considered in this analysis are shown in Table II. The *I–V* and *P–V* characteristics under different irradiation (two- and three-step change) and temperature conditions, as explained in Table II, are shown in Figs. 7 and 12.

The optimization of the string miniboost size is based on practical shading and lower irradiance profile, components cost and PV modules aging resulting in performance degradation. The miniboost component cost reduction aims for design optimization in cooling, magnetics, current sense transducer and power semiconductor devices, as it can be seen in Table III. The proposed peak power envelope operation provides optimal inverter operation by maximizing the utilization of the power components. The use of the proposed new methodology allows the PV inverter to operate at high efficiency while extending the operating range and keeping the system cost down.

The MPPT algorithm implemented is a perturb and observe with capabilities for detecting the global maximum using a periodic sweep. Other algorithms can be included to target specific needs given by the situation.

The sizing concept can be applied to a cost-performance optimization design, applicable to any PV system installation.

In the following section, experimental results of the proposed topology are presented in order to validate the system design.

TABLE II
CASE STUDY: SERIES- AND PARALLEL-CONNECTED PV MODULES WITH STEP-CHANGE IRRADIANCE

| Case | Irradiance distribution | | | | Converter topology | |
|---|---|---|---|---|---|---|
| | $Ns/G_1$ [no. PV]/ [$W/m^2$] | $Ns1/G_{21}$ [no. PV]/ [$W/m^2$] | $Ns2\,/\,G_{22}$ [no. PV]/ [$W/m^2$] | $Ns3/G_{23}$ [no. PV]/ [$W/m^2$] | Inverter without boost power stage | Inverter with miniboost power stages |
| C1 (see Fig. 7) | 19/1000 | 13/1000 | 6/600 | – | Limited power production. Shade intolerant. | MPPT power production. Shade tolerant. |
| C2 (see Fig. 8) | 19/1000 | 13/1000 | 6/400 | – | | |
| C3 (see Fig. 9) | 19/1000 | 13/800 | 6/600 | – | | |
| C4 (see Fig. 10) | 19/1000 | 13/800 | 6/400 | | | |
| C5 (see Fig. 11) | 19/1000 | 7/1000 | 6/600 | 6/200 | | |
| C6 (see Fig. 12) | 19/1000 | 7/800 | 6/400 | 6/100 | | |

PV module characteristics: $V_{\mathrm{oc.stc}} = 44.8\,\mathrm{V}$, $V_{\mathrm{MPP.stc}} = 36.3\,\mathrm{V}$, $I_{\mathrm{MPP.stc}} = 8.41\,\mathrm{A}$, $I_{\mathrm{SC.stc}} = 8.97\,\mathrm{A}$, $\beta = -0.34\%/^{\circ}\mathrm{C}$, $P_{\max} = 305\,\mathrm{W}$ (Canadian Solar CS6X-305P) with surface cell temperatures $T_c = -20, 0, 25, 50, 65, 80\,^{\circ}\mathrm{C}$ at $1^{\sim}\mathrm{kW/m^2}$. The 1000 V system has two parallel strings of 19 PV modules in series.

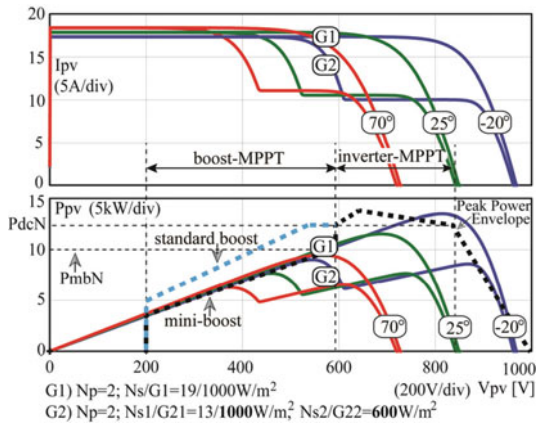


Fig. 7. Case C1: comparison between uniform irradiance $G1 = 1000$ W/m$^2$ and partially shaded $G2 = G_{21} = 1000 (Ns1 = 13)$, $G_{22} = 600$ (Ns2= 6) W/m$^2$. The solution with string miniboost is able to successfulcover the inverter operating regions.

TABLE III
BOOST DESIGN COMPARISON

| Parameter | Standard boost | String miniboost |
|---|---|---|
| Boost boundary maximum power, $P_{B\max}$ [p.u.] | 1 (12.5 kW) | 0.48 (6 kW) |
| Power gradient $m_B$ [W/V] | 26.7 | 17.5 |
| Maximum operating current ($I_{\mathrm{dcm}}$) [p.u.] | 1 (26.5 A) | 0.64 (17 A) |
| Power semiconductor devices ($Q$, $D_b$) sizing [p.u.] | 1 | 0.6 |
| Inductor ($L_b$) size [p.u.] | 1 | 0.7 |
| Current sensor ratings [p.u.] | 1 (40 A) | 0.625 (25 A) |

### *B. CM Circulating Current Issues and Improvement Solutions*

The inclusion of ZS triple harmonics components in three-phase converter's modulation ($m_{\max} = 2/\sqrt{3}$) provides extended dc-bus utilization that is 15% higher than the SPWM ($m_{\max} = 1$). As a result, the operation can be performed at a lower dc-bus voltage range, which leads to two advantages in terms of efficiency: lower switching losses (dc–ac inverter stage) and a lower conversion ratio between dc–dc boost and dc–ac inverter power stages.

In order to benefit from the above advantages, the three-phase 3L-TNPC considered in this work is designed with a neutral-point floating potential, i.e., the mid-point between top and bottom capacitors ($C_{zT}, C_{zB}$, Fig. 3). However, due to the nature of nongalvanic isolation between the PV modules and the grid, leakage currents are generated and propagated through the stray impedance (e.g., capacitance $C_{\mathrm{pv}.p}, C_{\mathrm{pv}.n}$ and resistance $R_{\mathrm{pv}.p}$, $R_{\mathrm{pv}.n}$, Fig. 3). The variability of the stray capacitance between the grounded PV module frame and the floating positive and negative terminals is mainly influenced by cell construction and weather conditions. In this case study, the stray capacitance is considered to have a value of 100 nF/kW.

The CM voltage is the sum of the phase voltages at each filter inductor terminal with respect to a common point (e.g., neutral-point ($z$) point, negative ($n$) and positive ($p$) dc terminals). The three-phase balanced voltage system and the CM voltage of the inverter output with respect to grid neutral ($N$) and neutral point ($z$) is expressed

$$\begin{cases} V_{aN} + V_{bN} + V_{cN} = 0 \\ V_{\mathrm{cm}.z} = \frac{V_{az} + V_{bz} + V_{cz}}{3}. \end{cases} \tag{19}$$

The voltage fluctuation at the dc positive and negative terminals becomes the generator source for the CM current. The circulation path formed through the PV stray capacitance and resistance ($C_{\mathrm{pv}}$, $R_{\mathrm{pv}}$) leads to CM current generation:

$$\begin{cases} \sum_{x=a,b,c} I_x = I_{\mathrm{cm}} \neq 0 \\ \left(I_x = I_{x.d} + \frac{I_{\mathrm{cm}}}{3}\right)|_{x=a,b,c}\ . \end{cases} \tag{20}$$

The phase output current contains the differential term ($I_{x.d}$), and one third of the CM current ($I_{\mathrm{cm}}$). The CM current magnitude is influenced by the PV stray impedance elements (e.g., $C_{\mathrm{pv}}$, $R_{\mathrm{pv}}$—leakage resistance provides a damping effect), the system components ($L_f$, $L_{\mathrm{cm.dc}}$, $L_{\mathrm{cm.ac}}$), the dc voltage operation ($V_{\mathrm{dc}}$), the modulation strategy and switching frequency impact on $dV_{C\mathrm{pv}}(t)/dt$:

$$i_{\mathrm{cm}}(t) = C_{\mathrm{pv}} \frac{dV_{C\mathrm{pv}}(t)}{dt}. \tag{21}$$

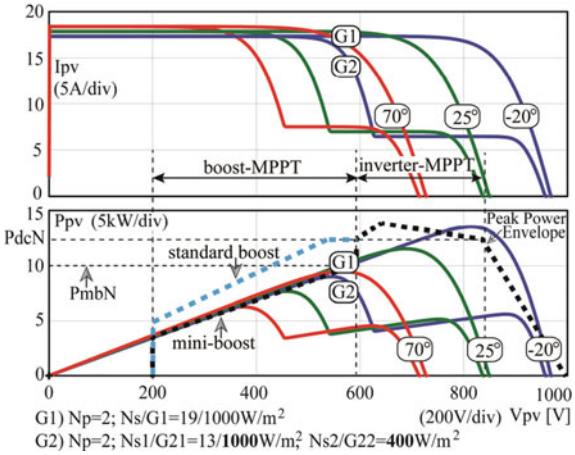


Fig. 8. Case C2: comparison between uniform irradiance $G1$= 1000 W/ m$^2$ and partially shaded $G2 = G_{21} = 1000$ (Ns1 = 13), $G_{22} = 400$ (Ns2 = 6)$W/m^2$. The solution with string miniboost is able to successful cover the inverter operating regions.

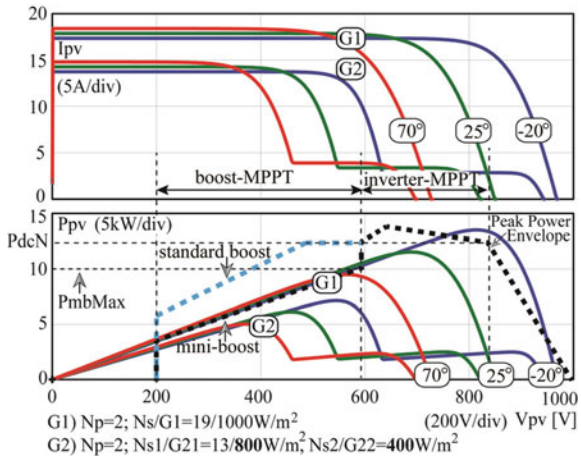


Fig. 10. Comparison between uniform irradiance $G1 = 1000$ W/m$^2$ and partially shaded $G2 = G_{21} = 800$ (Ns1= 13), $G_{22} = 400$ (Ns2= 6)$W/m^2$. The solution with string miniboost is able to successfully cover the inverter operating regions.

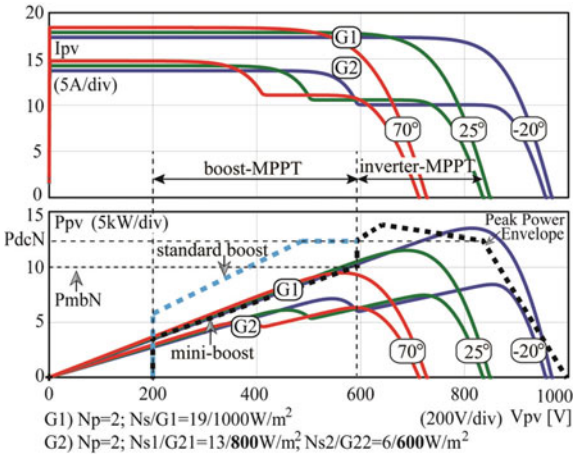


Fig. 9. Comparison between uniform irradiance $G1 = 1000$ W/m$^2$ and partially shaded $G2 = G_{21} = 800$(Ns1= 13), $G_{22} = 600$ (Ns2= 6)$W/m^2$. The solution with string miniboost is able to successfully cover the inverter operating regions.

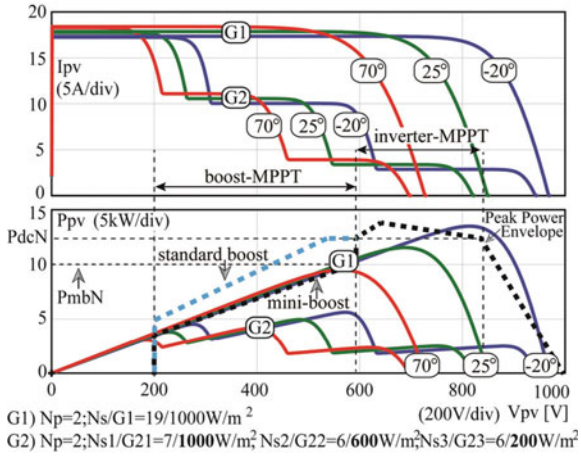


Fig. 11. Case C3: comparison between uniform irradiance $G1$= 1000 W/ m$^2$ and partially shaded $G2 = G_{21} = 1000(\mathrm{Ns1} = 7)$, $G_{22} = 600$ (Ns2= 6), $G_{23} = 200$ (Ns3 = 6) W/m$^2$. The solution with string miniboost is able to successfully cover the inverter operating regions.

The duration and magnitude of the leakage current above certain limits present a safety hazard by allowing the current to flow through the human body or to create fire hazards. The conditions for a current leakage and residual fault must occur when the current's value (RMS, average and sudden change) is above a permissible threshold (e.g., 300 mA, $P$<30 kVA, and 10 mA per kVA, $P$>30 kVA), which is usually determined by standards. The issue of CM (leakage) current reduction is addressed in this work using three different techniques: CM inductors, capacitive filtering, and modulation strategy.

The first technique reuses the dc and electromagnetic compliance (EMC) components ($L_{\mathrm{cm.dc}}$, $L_{\mathrm{cm.ac}}$, Fig. 3), which now are designed for a dual purpose: electromagnetic emissions (e.g., EN61000-6-3) and current leakage (e.g., IEC62109-2, VDE-AR-N-4105) compliance. This technique introduces high impedance in the leakage current path. Furthermore, an inductor ($L_{\mathrm{gnd}}$, Fig. 3) can be placed between the grid ground bonding and protective earth of the PV system. However, the ground inductor $L_{\mathrm{gnd}}$ has the disadvantage of increasing the cost of the system.

The second technique involves adding relatively low-cost film ac capacitors $(C_z)$, between the inverter output and neutral point (z). In this way, a fraction of $I_{\mathrm{cm}}$ is returned to its source and the leakage current circulation through the grid conductors is reduced.

The third technique is implemented at the three-phase inverter modulator level: while maintaining the ZS, the three-phase carriers are shifted as shown in Fig. 3. The concept introduced is a modified phase disposition (PD) modulation with a phase-shift (PS) angle ($\varphi$) between the inverter's three phases. Using this technique, the $dV_{C\mathrm{pv}}(t)/dt$ term from (21) is reduced in magnitude, and the end result is a lower CM voltage spectrum, with lower leakage current, as will be demonstrated in the next section.

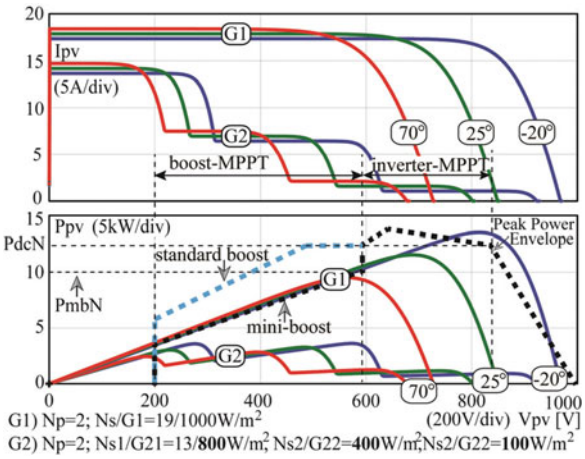


Fig. 12. Case C4: comparison between uniform irradiance $G1$= 1000 W/ m$^2$ and partially shaded $G2 = G_{21} = 800(\mathrm{Ns1} = 7)$, $G_{22} = 400(\mathrm{Ns2} = 6)$, $G_{23} = 100$ (Ns3 = 6) W/m$^2$. The solution with string miniboost is able to successfully cover the inverter operating regions.

TABLE IV
BOOST AND PV INVERTER MAIN CHARACTERISTICS

| Power stage | Nominal power $P_{\mathrm{dc}N}$, $P_n$ | Switching frequency | Power Inductor | DC operation range $V_{\mathrm{dcMin}}$–$V_{\mathrm{dcMax}}$ |
|---|---|---|---|---|
| stage | $P_{\mathrm{dc}N}$, $P_n$ [p.u.] | [kHz] | [mH] | [V] |
| Miniboost1 | 0.25 | 20 | $L_{b1} = 1$ | 200–850 |
| Miniboost2 | 0.25 | 20 | $L_{b2} = 1$ | 200–850 |
| Three-phase PV inverter | 1 | 20 | $L_f = 0.8$ | 575–850 |

## VI. SIMULATION AND EXPERIMENTAL RESULTS

An experimental setup was developed in order to evaluate the proposed architecture design for energy production on a three-phase 25-kVA inverter with dual string PV system. The characteristics of the experimental setup are presented in Table IV. As it can be observed, each miniboost stage is sized to 1/4 of the total rated power of the PV inverter, using components that are much smaller and more economical than the corresponding full-rated components for a 25 kW boost. The grid-connected PV inverter with dual miniboosts prototype configuration, used for experimental evaluation, is shown in Fig. 13. The sizing of the converter components was performed following the design procedure based on the optimized peak-power envelope in order to maximize the device utilization.

Fig. 14 shows the key waveforms of PV inverter operation with dual miniboosts using the proposed control structure from Fig. 3.

During the first interval $(t_0 - t_1)$, both miniboosts operate in independent MPPT mode, converting power from two separate and balanced PV arrays, $P_{\mathrm{pv1}} = P_{\mathrm{pv2}} = 2\,\mathrm{kW}$. At moment $t_1$, an imbalance is produced (sudden difference jump in irradiance on PV1 array), and MPPT1 (miniboost 1) detects an increase power available solely from PV1 array source and the total power generated is increased from 4 to 7 kW, which corresponds to the maximum power production available from PV arrays.

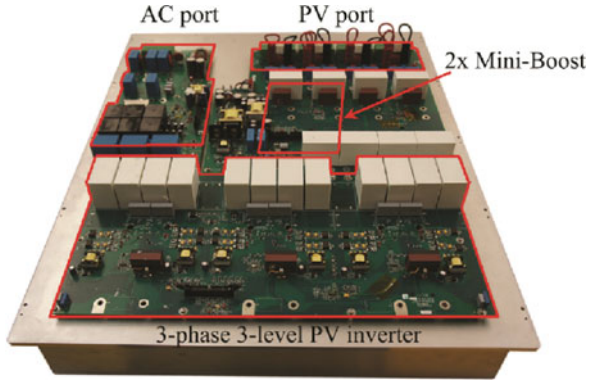


Fig. 13. Three-phase grid-connected PV inverter with string miniboosts prototype stage configuration for experimental evaluation.

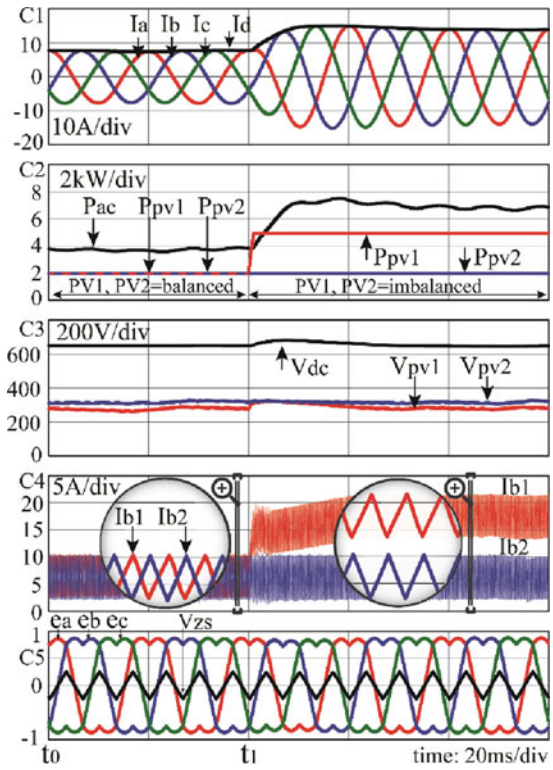


Fig. 14. Grid-connected PV inverter power conversion with dual miniboosts under balanced and imbalanced test cases: key waveforms.
*Y*-axis: C1—inverter phase currents $I_a$, $I_b$, $I_c$, and active current component $I_d$, 10 A/div. C2—boosts power, $P_{\mathrm{pv1}}$, $P_{\mathrm{pv2}}$, and inverter active power, $P_{\mathrm{ac}}$, 2 kW/div. C3—dc-link voltage $V_{\mathrm{dc}}$ and input voltages of two miniboost stages, $V_{\mathrm{pv1}}$, $V_{\mathrm{pv2}}$, 200 V/div. C4—Miniboosts inductor currents $I_{b1}$, $I_{b2}$, 5 A/div. C5—three-level three-phase control signals $e_a$, $e_b$, $e_c$ and ZS $V_{\mathrm{ZS}}$, 0.5 p.u./div. *X*-axis: 20 ms/div.

Part of the effectiveness of the inverter's control structure of Fig. 3 is demonstrated in the dynamics evaluation tests from Fig. 14.

Fig. 15 shows the grid-connected PV system's performance under step-load, i.e., PV array irradiance sudden profile change. In Fig. 15(a) and (b), prior to moment $t_0$, the two arrays PV1 and PV2 are exposed to a similar irradiance level. In this case, the miniboosts execute the MPPT algorithms ($V^*_{\mathrm{mppt1}}$, $V^*_{\mathrm{mppt2}}$,

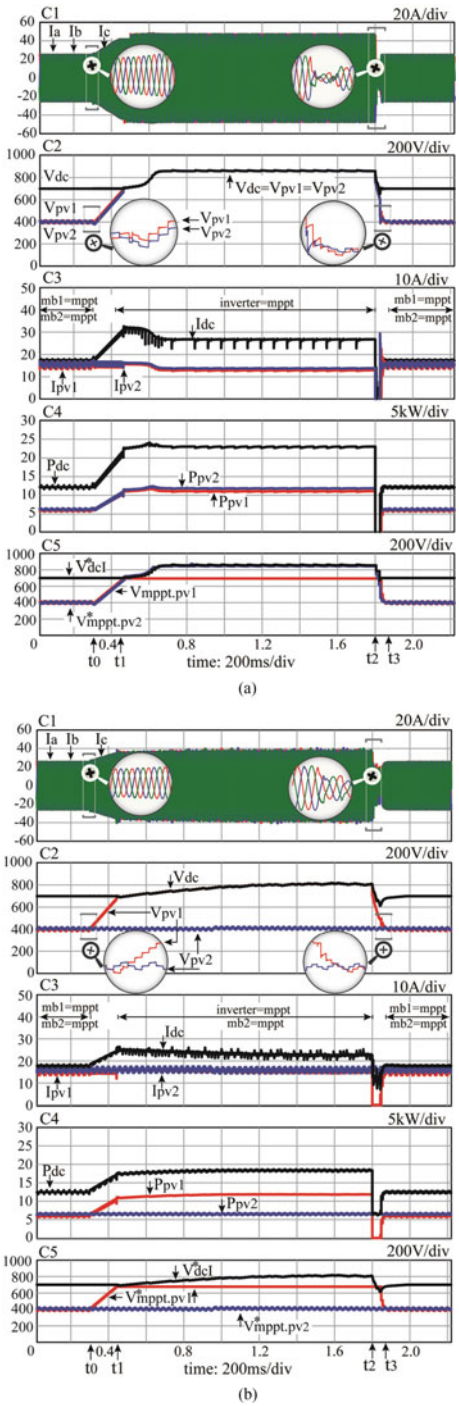


Fig. 15. Grid-connected PV inverter power conversion with dual miniboosts under two step-irradiance test cases. (a) System operation with MPPT transition from miniboost1 and miniboost2 to inverter stage. The PV1 and PV2 array characteristics are changed at $t_0$ as follows: $(I_{\rm mp1},\ V_{\rm mp1}, P_{\rm mp1}) = (15 \rightarrow 13\,{\rm A}, 400 \rightarrow 850\,{\rm V}, 6 \rightarrow 11\,{\rm kW})$ and $(I_{\rm mp2},\ V_{\rm mp2}, P_{\rm mp2}) = (15.5 \rightarrow 14.1\,{\rm A}, 400 \rightarrow 850\,{\rm V}, 6.2 \rightarrow 12\,{\rm kW})$. At $t_2$, PV1 and PV2 characteristics are returned to values prior to $t_0$. (b) System operation with MPPT transition from miniboost1 to inverter stage: PV1 array characteristics change $(I_{\rm mp1},\ V_{\rm mp1}, P_{\rm mp1}) = (15 \rightarrow 14.8\,{\rm A}, 400 \rightarrow 800\,{\rm V}, 6 \rightarrow 11.8\,{\rm kW})$ while PV1 remains constant $(I_{\rm mp2},\ V_{\rm mp2}, P_{\rm mp2}) = (15.5\,{\rm A}, 405\,{\rm V}, 6.27\,{\rm kW})$. At $t_2$, PV1 characteristics is returned to values prior to $t_0$. *Y*-axis: C1—inverter phase currents $I_a$, $I_b$, $I_c$, 20 A/div. C2—PV input voltages of two miniboost stages $V_{\rm pv1}$, $V_{\rm pv2}$, dc-link voltage $V_{\rm dc}$, 200 V/div. C3—PV input currents $I_{\rm pv1}$, $I_{\rm pv2}$, 10 A/div. C4—boosts power, $P_{\rm pv1}$, $P_{\rm pv2}$, and total dc power, $P_{\rm dc}$, 5 kW/div. C5—MPPT control signals (see Fig. 3), $V^*_{\rm mppt1}, V^*_{\rm mppt2}$, $V^*_{{\rm dc}I}$, 200 V/div. *X*-axis: 200 ms/div.

Fig. 3) while the inverter regulates the dc-link voltage ($V^*_{{\rm dc}I}$ Fig. 3).

Fig. 15(a) demonstrates the MPPT steady-state operation and transition of both miniboosts, from step-up conversion to bypass mode, where the MPPT is executed by the inverter stage. At the moment $t_0$, the available power at PV1 and PV2 ports suddenly approximately doubles. Consequently, the PV1 and PV2 voltages increase from $V_{\rm mp1} = 400\,{\rm V}$ (prior to $t_0$) until the MPP voltage is determined and settled by the inverter's MPPT algorithm. At $t_1$ the miniboosts transition to bypass mode and the task of tracking the maximum power is transferred to the inverter controls, regulating the dc-link voltage at $V_{\rm dc} = 850\,{\rm V}$. At $t_2$, the PV1 and PV2 characteristics return to their initial values prior to $t_0$ with stable transitions and, at $t_3$, the system resumes its initial operation.

Fig. 15(b) demonstrates the system's ability to operate flexibly using independent MPPT controls, fulfilled by the miniboosts and inverter conversion system. At the moment $t_0$, the available power at the PV1 port suddenly approximately doubles. As a result, the PV1 voltage increases from $V_{\rm mp1} = 400\,{\rm V}$ (prior to $t_0$) until the MPP voltage is determined and settled by the inverter's MPPT algorithm. At $t_1$, the miniboost transitions to bypass mode and the task of tracking the maximum power is transferred to the inverter controls, regulating the dc-link voltage at $V_{\rm dc} = 800\,{\rm V}$. At $t_2$, the PV1 characteristics returns to their initial values prior to $t_0$, while PV1 profile remains constant. The interchange of MPPT boosts-inverter functionality demonstrates the system's stability and robustness.

The experimental results of the inverter operation, with single- and two-stage, under dynamic and steady-state conditions for the MPPT arbitration are presented in Fig. 16–18.

The single-stage inverter operation is shown in Fig. 16 since the PV voltages, $(V_{\rm pv1}$ and $V_{\rm pv2}) > V_{\rm dcMin}$ are sufficient to bypass the miniboosts (case a, relation (8)). The MPPT is performed by inverter stage, with two PV strings balanced at 3.93 kW for power production. The MPPT perturbation (voltage steps from the control set-point $V^*_{{\rm dc}I}$, Fig. 3) is proportionally reflected in the dc components, $V_{\rm pv1}$, $V_{\rm pv2}$ and $V_{\rm dcMin}$ as it can be noted in Fig. 16(a). The inverter gradually increases the operating point of the converter until it reaches the 99.8% mark.

Fig. 17 shows the two-stage inverter conversion operation, with PV voltages $(V_{\rm pv1}$ and $V_{\rm pv2}) < V_{\rm dcMin}$ (case b, (8)). The two miniboost power stages are enabled due to low PV voltage operation. The MPPT perturbation (voltage steps from the control set-points $V^*_{\rm mppt1}, V^*_{\rm mppt2}$, Fig. 3) is independently performed by the two miniboosts as it can be observed in waveforms $V_{\rm pv1}$ and $V_{\rm pv2}$ in Fig. 17(a).

A single-stage PV inverter (without miniboost) would not be able to operate under these conditions since the voltage is less than the required $V_{\rm dcMin} = 575\,{\rm Vdc}$ (e.g., $230\,{\rm V_{LN}}/400{\rm V_{LL}}$ grid).

In Fig. 18, the experimental results with an imbalance of power between two independent PV input strings (Fig. 3, miniboost 1 and 2 with conduction diodes $D_{p1}$, $D_{p2}$) are shown. This case corresponds for the case with different ori-

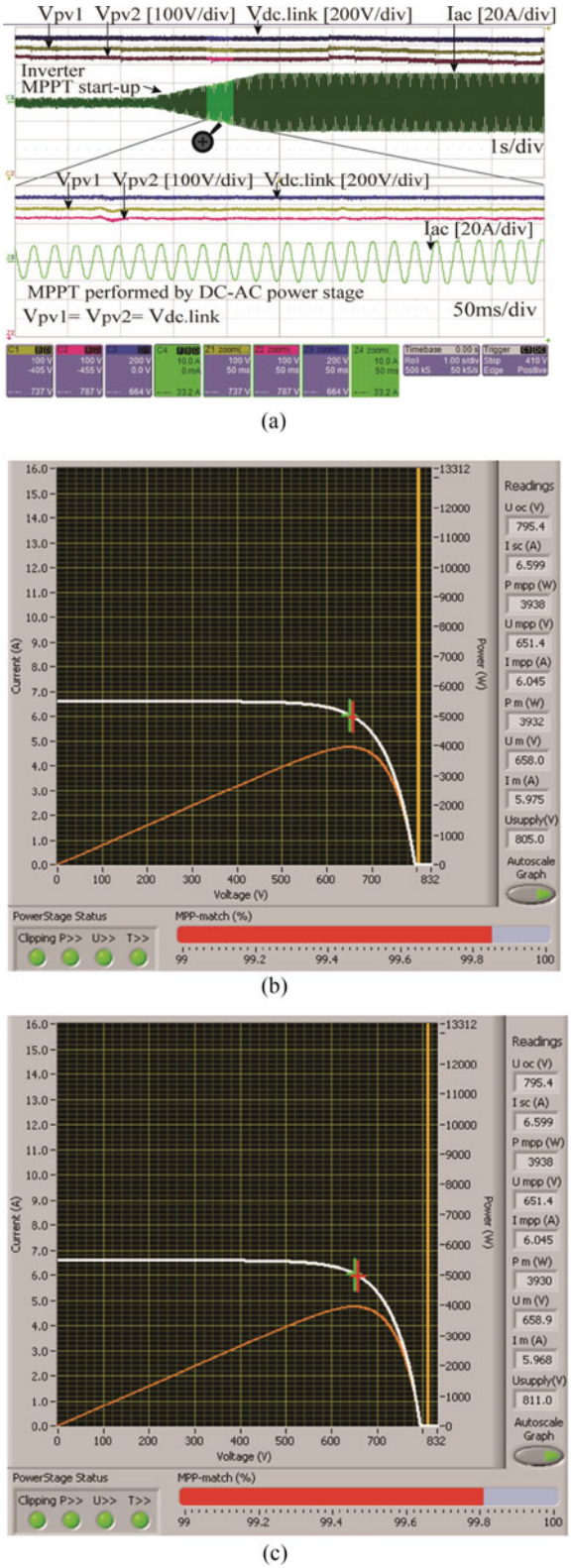


Fig. 16. Single-stage PV inverter operation (miniboosts are switched automatically off). The MPPT is performed by the inverter $(V_{\mathrm{pv1}}$ and $V_{\mathrm{pv2}}) > V_{\mathrm{dcMin}}$. Experimental results with inverter–MPPT control dynamics under irradiance-power change: 1–8 kW, grid-connected three-phase 230/400 V–50 Hz. PV1: *I–V*, *P–V* characteristics with inverter-MPPT algorithm efficiency of 99.8%.

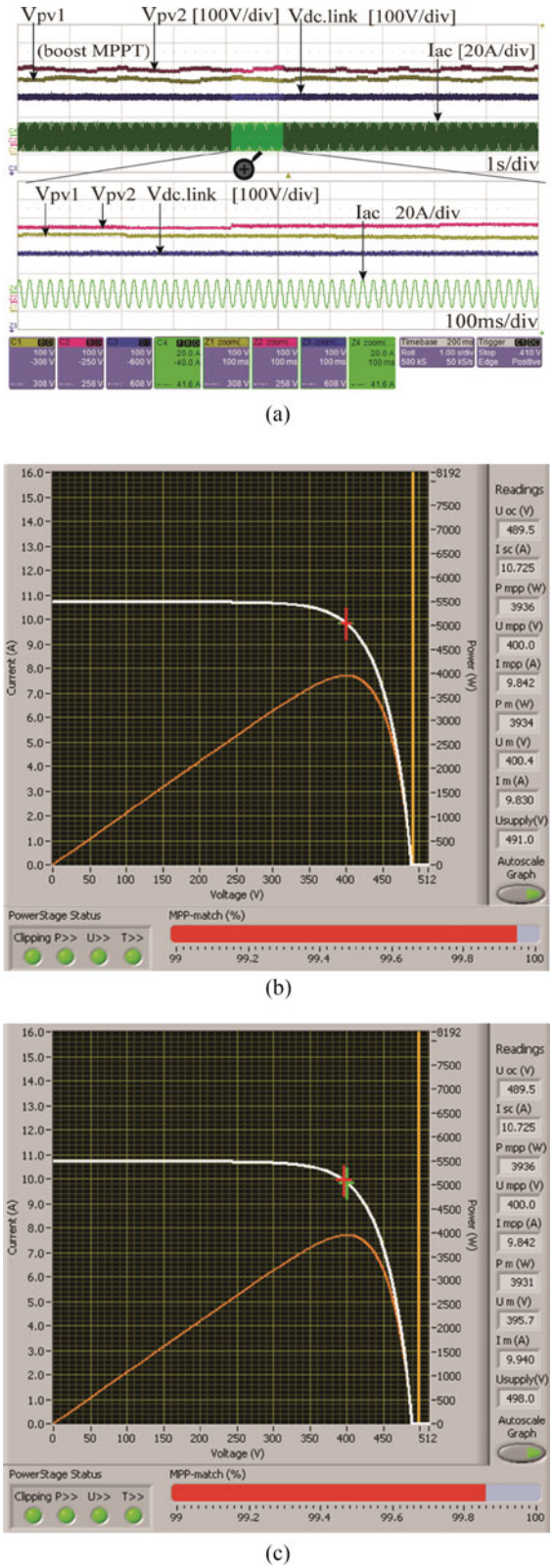


Fig. 17. Two-stage PV inverter operation, with two miniboost engaged (PV1 and PV2). The MPPT is performed by two miniboosts $(V_{\mathrm{pv1}}$ and $V_{\mathrm{pv2}}) < V_{\mathrm{dcMin}}$. Experimental results with string miniboosts-MPPT under steady-state conditions with 7.6 kW grid power production, with MPPT algorithm efficiency of 99.8%.

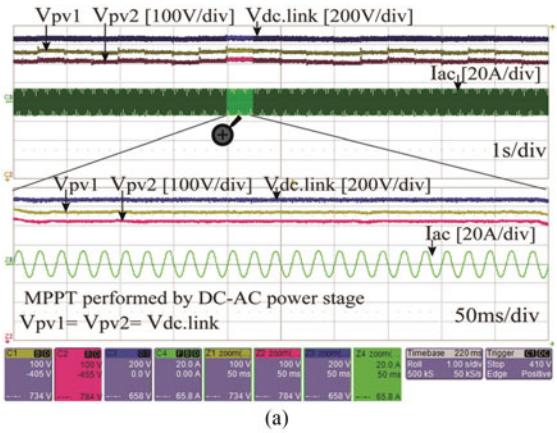


(a)

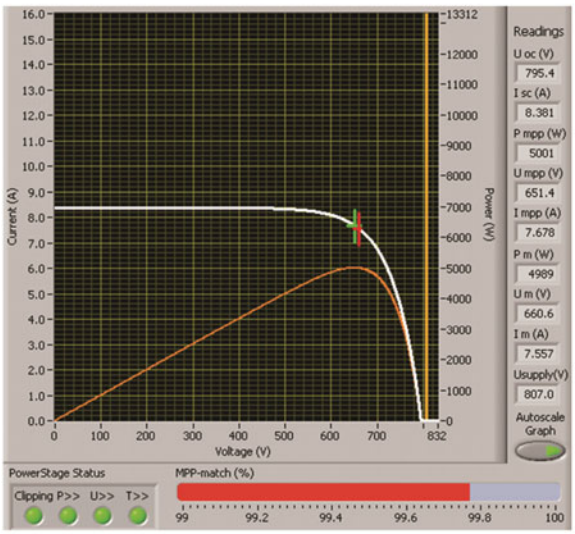


(b)

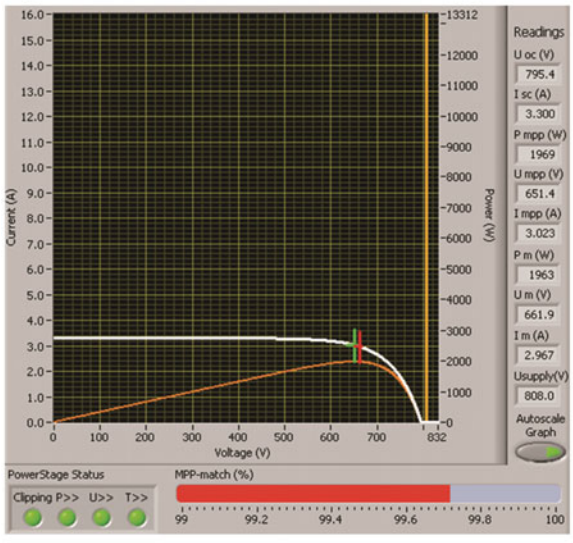


(c)

Fig. 18. Single-stage PV inverter operation (miniboosts are switched automatically off). Inverter MPPT-control dynamics under imbalanced PV input strings loading: 5 and 1.96 kW, grid-connected three-phase 230/400 V–50 Hz. PV1: *I–V*, *P–V* characteristics with inverter-MPPT algorithm efficiency of 99.7% (miniboost = off with $D_{p1},\ D_{p2} = \text{on}$).

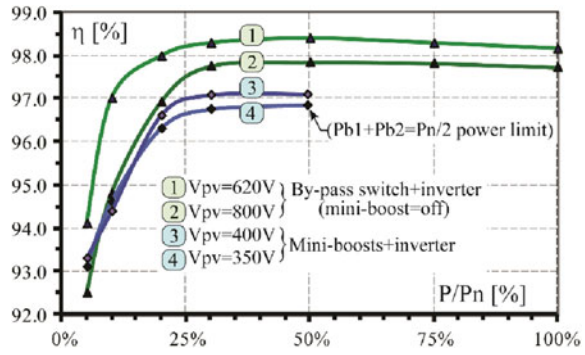


Fig. 19. Power conversion efficiency measurements: (1), (2) are with bypass switch and dc–ac inverter and (3), (4) are with two miniboosts (each rated at $P_n/4$) and dc–ac inverter. The auxiliary system power consumption is included: electromagnetic interference filters, cooling fans, ac disconnect relays, signal conditioning. Test conditions: unity power factor $(\text{PF} = 1)$, $230\,\text{V}_{\text{LN}}/400\,\text{V}_{\text{LL}}$, 50 Hz, $P_n = 25\,\text{kVA}$.

TABLE V
SYSTEM DESIGN PARAMETERS

| Description | Symbol | Value |
|---|---|---|
| Boost diode voltage drop ($I_f$ = 16 A, $T_j = 100\,^\circ\text{C}$) | $V_f\,(D_{b1,2})$ (type: silicon carbide) | 1.8 V ($P_{bp} = 2P_d =$ 57.6 W) |
| By-pass diode voltage drop ($I_f$ = 16 A, $T_j = 100\,^\circ\text{C}$) | $V_f\,(D_{p1,2})$ (type: standard recovery) | 0.825 V ($P_{bp} =$ $2P_d = 26.4$ W) |
| Bypass switch resistance | $R_f\,(k_{p1,2})$ (type: relay) | 10 mΩ ($P_{bp} =$ $2P_d = 5.12$ W) |
| Rated power (PF = 1) | $P_n$ | 25 kW |
| PV operating voltage | $V_{\text{pv1}} = V_{\text{pv1}} = V_{\text{dc}}$ | 800 V |
| PV stray capacitance | $C_{\text{pv}} = \sum^{C_{\text{pv},p,n}}$. | 2.5 μF |
| PV stray resistance | $R_{\text{pv.equivalent}}$ | 1 Ω |
| AC filter | $C_f$ | 10 μF |
| CM ac neutral-point filter | $C_z$ | 4.7 μF |
| CM dc filter | $L_{\text{cm.dc}}$ | 2 mH |
| CM ac filter | $L_{\text{cm.ac}}$ | 1.5 mH |
| Differential ground filter | $L_{\text{gnd}}$ | 1 mH |
| Grid impedance | $Z_g = R_g + j\omega L_g$ | [0.1+$j\omega$(0.1 mH)] Ω |
| Maximum CM current (Limits imposed by safety standards) | $I_{\text{cm.max}}$ | $300\,\text{mA}_{\text{rms}}$ (detection time: 0.3 s) |

entation of PV modules (e.g., rooftops angle) fixed typical position, without the capability to track the sun throughout the day. The inverter-MPPT algorithm performs periodic voltage sweeps in order to determine the global maxima for optimal energy production. The miniboost is able to increase the dc voltage to the operating point for improved PV inverter energy production, with reduced size and power rating components.

Fig. 19 shows the power conversion system's efficiency, where higher performance is achieved when the boost stages are switched off, i.e., when using a bypass switch and dc–ac inverter, especially at higher modulation index (e.g., 620 V, curve (1)) operation.

Table V shows the bypass switch design comparison and the necessary design parameters for the CM current circulation reduction evaluation.

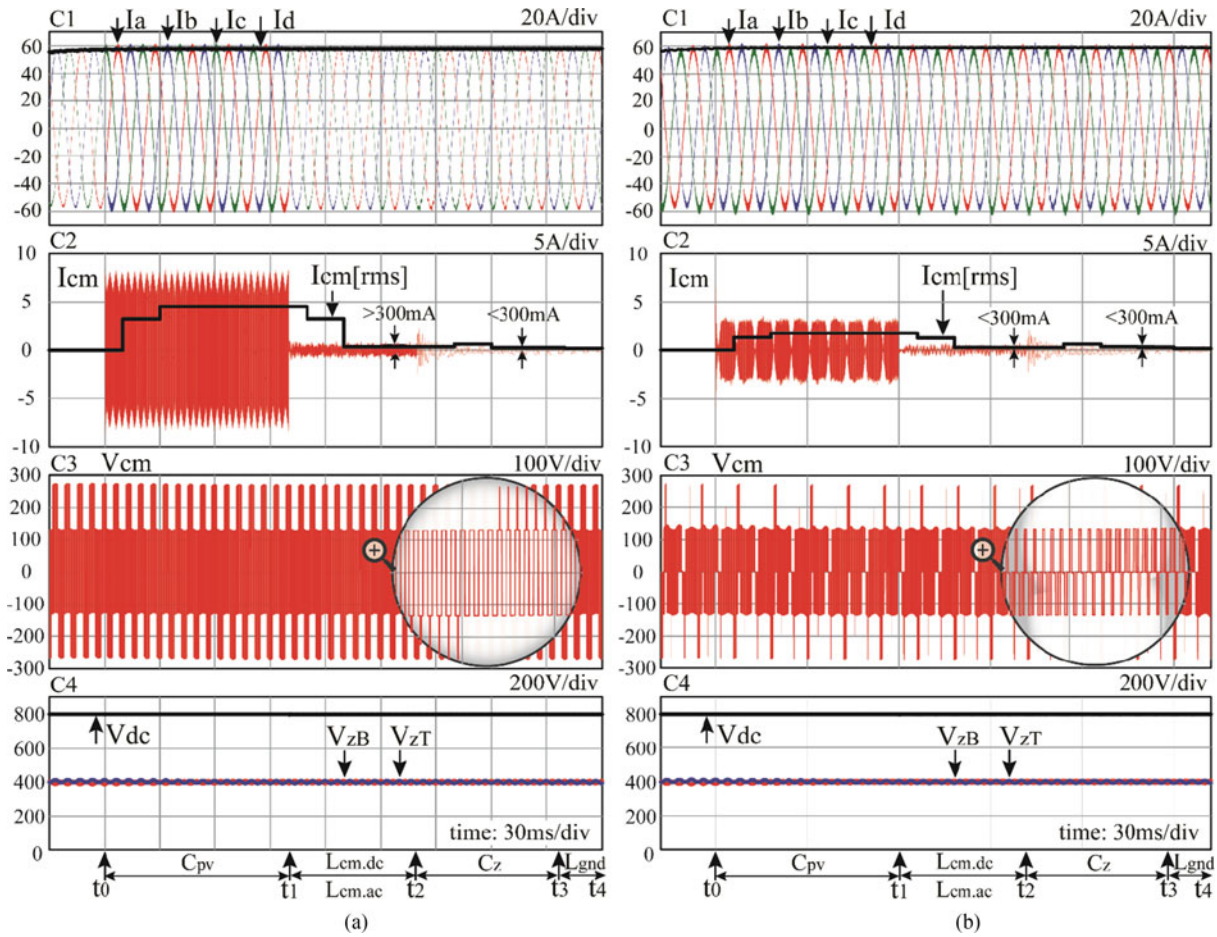


Fig. 20. CM current reduction techniques: (a) PD modulation and modified PD-PS ($\varphi_A = 0, \varphi_B = \pi/2, \varphi_C = \pi$) strategies comparison. *Y*-axis: C1—inverter phase currents $I_a$, $I_b$, $I_c$, and active current component $I_d$, 20 A/div. C2—CM (leakage) circulating current, $I_{\rm cm}$, 5 A/div. C3—CM voltage waveform with respect to neutral-point (*z*) (see (17) and Fig. 3), $V_{\rm cm}$, 200 V/div. C4—dc-link voltage $V_{\rm dc}$, and bottom and top voltages with active neutral-point regulation control, $V_{zB}$, $V_{zT}$, 200 V/div. *X*-axis: 30 ms/div. Test conditions: $V_{\rm pv1} = V_{\rm pv2} = V_{\rm dc} = 800\,{\rm V}$ (bypass mode), $PF = 1$, $230\tilde{}{\rm V_{LN}}/400\tilde{}{\rm V_{LL}}$, 50 Hz, $P_n = 25\,{\rm kVA}$.

TABLE VI
PARAMETERS OF THE SIMULATION EVALUATION

| Time interval | Improvement solution | Modulation strategy | $I_{\rm cm}$ $[A_{\rm rms}]$ | $I_{\rm cm} < 300\,{\rm mA}$ |
|---|---|---|---|---|
| $t_0 - t_1$ | None | PD | 4.53 | No |
| | | PD-PS | 1.78 | No |
| $t_1 - t_2$ | $L_{\rm cm.dc} + L_{\rm cm.ac}$ | PD | 0.357 | No |
| | | PD-PS | 0.255 | Yes |
| $t_2 - t_3$ | $C_z$ | PD | 0.202 | Yes |
| | | PD-PS | 0.158 | Yes |
| $t_3 - t_4$ | $L_{\rm gnd}$ | PD | 0.186 | Yes |
| | | PD-PS | 0.155 | Yes |

To present a practical and relevant example, when using a low voltage-drop diode ($D_{p1,2}$), the bypass losses ($P_{bp}$) are 50% lower than the bypass losses produced when the boost diode ($D_{b1,2}$) is used. Further improvement is obtained by using a low-cost relay ($k_{p1,2}$), which reduces the losses by 90%, as shown in Table V. Evidently, the bypass switch design has significant consequences for power dissipation ($P_{bp}$), which affects system cooling and efficiency.

The investigation of circulating CM current uses the design parameters from Table V. The evaluation is conducted at high dc operating voltages (e.g., 800 V) where the leakage current attains maximum values (due to $dV_{C\rm pv}(t)/dt$ term from (19)).

Fig. 20 shows the inverter operating with (a) PD and (b) modified phase-disposition phase-shift (PD-PS) modulation strategies. In both modulation cases, the CM is measured under four identical test cases, as specified in Table VI. Prior to moment $t_0$, an ideal case is considered, without stray capacitance, where the CM current is zero, as per (21). At $t_0$, the stray capacitance $C_{\rm pv}$ is suddenly connected (see Fig. 3) resulting in a leakage current of approximately $12\%\ I_n$ [see Fig. 20(a)]. The connection of the stray capacitance is also reflected in the inverter output current, as per (20). The modified PD-PS modulation provides a better performance, with a leakage current of $5\%\ I_n$. However, even this value is over the maximum continuous current limit (e.g., 300 mA).

The test continues with the insertion ($t_1$) of EMC filter components, $L_{\rm cm.dc}$, $L_{\rm cm.ac}$, which dramatically reduces the CM current. Under these conditions, the grid-connected PV

system is standards-compliant only when using PD-PS modulation technique, as can be seen in Fig. 20(b) and Table VI. Using the standard PD modulation, the CM current is still over the required limit, as shown in Fig. 20(a) and Table VI. Further CM current improvement is achieved by connecting, at $t_2$, an impedance branch ($C_z$) from the inverter output to the common neutral-point (z), as shown in Fig. 3. In this way, a fraction (value dependent of $C_z$) of CM current circulates back to the source through this newly inserted path. As a result, the leakage current is reduced and the PV system is compatible with both modulation strategies. The last test occurs at $t_3$, where a ground inductor is enabled in the CM current path for further leakage current attenuation.

## VII. Conclusion

A graphical approach using *I–V* and *P–V* characteristics provided remarkable insights interactions of the PV–converter system. A new architecture for PV grid-connected converters based on a string miniboost stage to increase the operating region of the inverter without the losses and cost of a full size boost stage was introduced in this paper. In essence, the miniboost is a PV string boost converter equipped with an efficient bypass switch element. The PV string boost concept is developed in design size optimization, for the typical PV modules used worldwide. The design optimization maximizes the utilization of the power components by using the proposed peak power envelope inverter operation and only engaging the miniboost when necessary given the array conditions.

The proposed architecture kept the advantages of the current single-stage PV inverter (increased efficiency using a bypass switch) when the PV voltage was high enough avoiding the use of the miniboost and allowed the operation when the PV array voltage dropped below the minimum voltage, likely due to partial shading phenomena. The proposed topology was composed of one or more boost stages rated for a fraction of the nominal power of the PV inverter connected to each string of the PV array that could be bypassed if the PV string met the voltage requirements of the PV inverter by itself, avoiding the losses when the additional boosting is not needed and limiting the cost. Individual miniboost stages could be used for multistring PV arrays reducing the possibility of operation at local maxima and providing improved energy extraction capabilities. The proposed inverter peak power envelope at boundary conversion operation provides design optimization for energy production maximization. Three methods of CM reduction for safety and standards-compliance were discussed. The overall performance and the utilization of the PV array and PV inverter were improved by the use of this topology and design methodology novel approach.

Experimental results using a three-phase 25-kVA inverter with dual string PV system and the same inverter with two string miniboost stages were presented showing the advantages for improved energy production of the proposed new architecture.

## References


[1] E. Serban, M. Ordonez, and C. Pondiche, "DC-bus voltage range extension in 1500 V photovoltaic inverters," *IEEE J. Emerg. Sel. Topics Power Electron.*, vol. 3, no. 4, pp. 901–917, Dec. 2015.

[2] M. Schweizer and J. Kolar, "Design and implementation of a highly efficient three-level t-type converter for low-voltage applications," *IEEE Trans. Power Electron.*, vol. 28, no. 2, pp. 899–907, Feb. 2013.

[3] T. Soeiro and J. Kolar, "The new high-efficiency hybrid neutral-point-clamped converter," *IEEE Trans. Ind. Electron.*, vol. 60, no. 5, pp. 1919–1935, May 2013.

[4] N.-C. Sintamarean, F. Blaabjerg, H. Wang, and Y. Yang, "Real field mission profile oriented design of a SiC-based PV-inverter application," *IEEE Trans. Ind. Appl.*, vol. 50, no. 6, pp. 4082–4089, Nov./ Dec. 2014.

[5] F. Blaabjerg, R. Teodorescu, M. Liserre, and A. V. Timbus, "Overview of control and grid synchronization for distributed power generation systems," *IEEE Trans. Ind. Electron.*, vol. 53, no. 5, pp. 1398–1409, Oct. 2006.

[6] J. I. Leon, L. G. Franquelo, B. Wu, and S. Kouro, "Introduction to the special section on modulation techniques for dc-to-ac power converters," *IEEE Trans. Ind. Electron.*, vol. 60, no. 5, pp. 1859–1860, May 2013.

[7] K. Ma and F. Blaabjerg, "Modulation methods for neutral-point-clamped wind power converter achieving loss and thermal redistribution under low-voltage ride-through," *IEEE Trans. Ind. Electron.*, vol. 61, no. 2, pp. 835–845, Feb. 2014.

[8] S. Vazquez, J. A. Sanchez, M. R. Reyes, J. I. Leon, and J. M. Carrasco, "Adaptive vectorial filter for grid synchronization of power converters under unbalanced and/or distorted grid conditions," *IEEE Trans. Ind. Electron.*, vol. 61, no. 3, pp. 1355–1367, Mar. 2014.

[9] R. Teodorescu, M. Liserre, and P. Rodriguez, *Grid Converters for Photovoltaic and Wind Power Systems*. New York, NY, USA: Wiley, 2011.

[10] E. Romero-Cadaval, G. Spagnuolo, L. G. Franquelo, C. A. Ramos-Paja, T. Suntio, and W. M. Xiao, "Grid-connected photovoltaic generation plants: Components and operation," *IEEE Ind. Electron. Mag.*, vol. 7, no. 3, pp. 6–20, Sep. 2013.

[11] E. Roman, R. Alonso, P. Ibanez, S. Elorduizapatarietxe, and D. Goitia, "Intelligent PV module for grid-connected PV systems," *IEEE Trans. Ind. Electron.*, vol. 53, no. 4, pp. 1066–1073, Jun. 2006.

[12] N. Femia, G. Petrone, G. Spagnuolo, and M. Vitelli, *Power Electronics and Control Techniques for Maximum Energy Harvesting in Photovoltaic Systems*, 1st ed. Boca Raton, FL, USA: CRC Press, 2012.

[13] F. Spertino and J. S. Akilimali, "Are manufacturing *I–V* mismatch and reverse currents key factors in large photovoltaic arrays?" *IEEE Trans. Ind. Electron.*, vol. 56, no. 11, pp. 4520–4531, Nov. 2009.

[14] Y.-J. Wang and P.-C. Hsu, "Analytical modelling of partial shading and different orientation of photovoltaic modules," *IET Renewable Power Gener.*, vol. 4, no. 3, pp. 272–282, 2010.

[15] C. Konstantopoulos and E. Koutroulis, "Global maximum power point tracking of flexible photovoltaic modules," *IEEE Trans. Power Electron.*, vol. 29, no. 4, pp. 2817–2828, Jun. 2014.

[16] D. Sera, R. Teodorescu, J. Hantschel, and M. Knoll, "Optimized maximum power point tracker for fast-changing environmental conditions," *IEEE Trans. Ind. Electron.*, vol. 55, no. 7, pp. 2629–2637, Jul. 2008.

[17] D. Sera, L. Mathe, T. Kerekes, S. Spataru, and R. Teodorescu, "On the perturb-and-observe and incremental conductance MPPT methods for PV systems," *IEEE J. Photovolt.*, vol. 3, no. 3, pp. 1070–1078, Jul. 2013.

[18] M. A. G. de Brito, L. Galotto, L. P. Sampaio, G. de Azevedo e Melo, and C. A. Canesin, "Evaluation of the main MPPT techniques for photovoltaic applications," *IEEE Trans. Ind. Electron.*, vol. 60, no. 3, pp. 1156–1167, Nov. 2013.

[19] M. Drif, P. Prez, J. Aguilera, and J. Aguilar, "A new estimation method of irradiance on a partially shaded {PV} generator in grid-connected photovoltaic systems," *Renewable Energy*, vol. 33, no. 9, pp. 2048–2056, 2008.

[20] A. Bidram, A. Davoudi, and R. S. Balog, "Control and circuit techniques to mitigate partial shading effects in photovoltaic arrays," *IEEE J. Photovolt.*, vol. 2, no. 4, pp. 532–546, Oct. 2012.

[21] B. N. Alajmi, K. H. Ahmed, S. J. Finney, and B. W. Williams, "A maximum power point tracking technique for partially shaded photovoltaic systems in microgrids," *IEEE Trans. Ind. Electron.*, vol. 60, no. 4, pp. 1596–1606, Apr. 2013.

[22] N. Mutoh, M. Ohno, and T. Inoue, "A method for MPPT control while searching for parameters corresponding to weather conditions for PV generation systems," *IEEE Trans. Ind. Electron.*, vol. 53, no. 4, pp. 1055–1065, Jun. 2006.

[23] G. Carannante, C. Fraddanno, M. Pagano, and L. Piegari, "Experimental performance of MPPT algorithm for photovoltaic sources subject to inhomogeneous insolation," *IEEE Trans. Ind. Electron.*, vol. 56, no. 11, pp. 4374–4380, Nov. 2009.
[24] T. L. Nguyen and K.-S. Low, "A global maximum power point tracking scheme employing direct search algorithm for photovoltaic systems," *IEEE Trans. Ind. Electron.*, vol. 57, no. 10, pp. 3456–3467, Oct. 2010.
[25] Y.-H. Ji, D.-Y. Jung, J.-G. Kim, J.-H. Kim, T.-W. Lee, and C.-Y. Won, "A real maximum power point tracking method for mismatching compensation in PV array under partially shaded conditions," *IEEE Trans. Power Electron.*, vol. 26, no. 4, pp. 1001–1009, Apr. 2011.
[26] E. Koutroulis and F. Blaabjerg, "A new technique for tracking the global maximum power point of PV arrays operating under partial-shading conditions," *IEEE J. Photovolt.*, vol. 2, no. 2, pp. 184–190, Apr. 2012.
[27] T. Kerekes, R. Teodorescu, M. Liserre, C. Klumpner, and M. Sumner, "Evaluation of three-phase transformerless photovoltaic inverter topologies," *IEEE Trans. Power Electron.*, vol. 24, no. 9, pp. 2202–2211, Sep. 2009.
[28] M. C. Cavalcanti, K. C. de Oliveira, A. M. de Farias, F. A. S. Neves, G. M. S. Azevedo, and F. C. Camboim, "Modulation techniques to eliminate leakage currents in transformerless three-phase photovoltaic systems," *IEEE Trans. Ind. Electron.*, vol. 57, no. 4, pp. 1360–1368, Apr. 2010.
[29] M. C. Cavalcanti, A. M. Farias, K. C. Oliveira, F. A. S. Neves, and J. L. Afonso, "Eliminating leakage currents in neutral point clamped inverters for photovoltaic system," *IEEE Trans. Ind. Electron.*, vol. 59, no. 1, pp. 435–443, Jan. 2012.
[30] X. Guo, M. C. Cavalcanti, A. M. Farias, and J. M. Guerrero, "Single-carrier modulation for neutral-point-clamped inverters in three-phase transformerless photovoltaic systems," *IEEE Trans. Power Electron. Lett.*, vol. 28, no. 6, pp. 2635–2637, Jun. 2013.

**Emanuel Serban** (M'99–SM'09) received the B.Sc. and M.Sc. degrees in electrical engineering from the University Politehnica of Timisoara, Timi'oara, Romania, in 1994 and 1995, respectively. He is currently working toward the Ph.D. degree in the Department of Electrical Engineering and Computing Science, University of British Columbia, Vancouver, BC, Canada.

In 1997, he joined Xantrex Technology, Inc., where he developed several power electronics platforms for industry and renewable backup applications. Since 2009, he has been with the Solar Business at Schneider Electric, Vancouver, where he is Research & Development Chief Engineer, Power Electronics Design, responsible for hybrid distributed power systems, renewable multilevel converters architecture and platform design. He developed single-phase and three-phase converter platforms for residential and commercial solar and electrical energy storage applications. His main fields of interest are in power electronics modeling and control, analysis and design of power converters for renewable, electrical storage and distributed energy systems.

**Francisco Paz** (S'08) was born in La Plata, Argentina. He received the Ing. degree in electronics engineering from the National University of Comahue, Neuquén, Argentina, in 2012. He began research activities that same year at the University of British Columbia (UBC), Vancouver, BC, Canada, where he received the M.A.Sc. degree in electrical engineering in 2014, and also working toward the Ph.D. degree in the same university.

His current interests include renewable energy conversion, maximum power point tracking and renewable energy system topologies for solar, wind and marine power.

Mr. Paz was recognized with several scholarships, including one from the Argentinian Ministry of Education, Science, Technology and Productive Innovation (2008), the ICICS Graduate Scholarship (2014), the Faculty of Applied Science Graduate Award (The University of British Columbia, 2014, 2015, and 2016), and the Four Year Fellowship for Ph.D. students (2014) from UBC.

**Martin Ordonez** (S'02–M'09) was born in Neuquen, Argentina. He received the Ing. degree in electronics engineering from the National Technological University, Cordoba, Argentina, in 2003, and the M.Eng. and Ph.D. degrees in electrical engineering from the Memorial University of Newfoundland (MUN), St. John's, NL, Canada, in 2006 and 2009, respectively.

He is currently the Canada Research Chair in power converters for renewable energy systems and an Associate Professor in the Department of Electrical and Computer Engineering, University of British Columbia (UBC), Vancouver, BC, Canada. He is also the holder of the Fred Kaiser Professorship on Power Conversion and Sustainability at UBC. He was an Adjunct Professor with Simon Fraser University, Burnaby, BC, Canada, and MUN. His industrial experience in power conversion includes research and development at Xantrex Technology, Inc./Elgar Electronics Corp. (now AMETEK Programmable Power, San Diego, CA, USA), Deep-Ing Electronica de Potencia (Rosario, Argentina), and TRV Dispositivos (Cordoba, Argentina). With the support of industrial funds and the Natural Sciences and Engineering Research Council, he has contributed to more than 100 publications and R&D reports.

Dr. Ordonez is an Associate Editor of the IEEE TRANSACTIONS ON POWER ELECTRONICS, a Guest Editor for IEEE JOURNAL OF EMERGING AND SELECTED TOPICS IN POWER ELECTRONICS, an Editor for IEEE TRANSACTIONS ON SUSTAINABLE ENERGY serves on several IEEE committees, and reviews widely for IEEE/IET journals and international conferences. He received the David Dunsiger Award for Excellence in the Faculty of Engineering and Applied Science (2009) and the Chancellors Graduate Award/Birks Graduate Medal (2006), and became a Fellow of the School of Graduate Studies, MUN.